Plasmonic lattice Kerker effect in ultraviolet-visible spectral range

V. S. Gerasimov,[1,2,*] A. E. Ershov,[1,2] R. G. Bikbaev,[1,3] I. L. Rasskazov,[4] I. L. Isaev,[2] P. N. Semina,[1] A. S. Kostyukov,[1] V. I. Zakomirnyi,[1,2] S. P. Polyutov,[1,†] and S. V. Karpov[1,3]

[1]*Siberian Federal University, Krasnoyarsk, 660041, Russia*

[2]*Institute of Computational Modelling of the Siberian Branch of the Russian Academy of Sciences, Krasnoyarsk, 660036, Russia*

[3]*L. V. Kirensky Institute of Physics, Federal Research Center KSC SB RAS, Krasnoyarsk, 660036, Russia*

[4]*The Institute of Optics, University of Rochester, Rochester, New York 14627, USA*

(Received 27 August 2020; revised 28 November 2020; accepted 2 December 2020; published 5 January 2021)

Mostly forsaken, but revived after the emergence of all-dielectric nanophotonics, the Kerker effect can be observed in a variety of nanostructures from high-index constituents with strong electric and magnetic Mie resonances. A necessary requirement for the existence of a magnetic response limits the use of generally nonmagnetic conventional plasmonic nanostructures for the Kerker effect. In spite of this, we demonstrate here the emergence of the lattice Kerker effect in regular plasmonic Al nanostructures. Collective lattice oscillations emerging from the delicate interplay between Rayleigh anomalies and localized surface plasmon resonances both of electric and magnetic dipoles, and electric and magnetic quadrupoles result in suppression of the backscattering in a broad spectral range. Variation of geometrical parameters of Al arrays allows for tailoring the lattice Kerker effect throughout UV and visible wavelength ranges, which is close to impossible to achieve using other plasmonic or all-dielectric materials. It is argued that our results set the ground for wide ramifications in the plasmonics and further application of the Kerker effect.

DOI: 10.1103/PhysRevB.103.035402

I. INTRODUCTION

The concept of backscattering suppression of light by a single spherical particle was proposed over three decades ago by Kerker *et al.* [1] The essential pre-requisite for this effect is the equivalence of permittivity and permeability of a sphere, $\varepsilon = \mu$, which implies a co-existence of pronounced electric and magnetic responses at the same frequency. This exciting idea did not receive a lot of attention in the past because such materials are close to impossible to find in nature. However, the situation has changed dramatically with the emergence of all-dielectric nanophotonics [2]. Optically induced magnetic moments mediate so-called "artificial magnetism" [3], which surpasses the requirement for the material to exhibit conventional magnetic properties. Thus, experimental evidence of the Kerker effect has been provided for single high-index Si [4] or GaAs [5] nanoparticles (NPs). After these pioneering experimental observations, the Kerker effect has been demonstrated in numerous setups [6–16] with a promising applications in a variety of endeavors such as sensing [17], imaging [18], and others [19]. These advances of all-dielectric nanophotonics left plasmonics much in a shadow. The inherently weak magnetic response of metal NPs, together with losses makes it difficult [20] yet possible [21] to harness the Kerker effect in single plasmonic NPs. Moreover, different combinations of plasmonic materials with all-dielectric [22,23] or magnetic [24] structures may satisfy the Kerker condition.

On a larger scale, i.e., in arrays of NPs, the Kerker effect can be implemented via collective lattice resonances (CLRs) [25,26]. CLRs emerging in arrays of both plasmonic [27–30] and all-dielectric [31–33] NPs are high-quality modes originating from the coupling between Rayleigh anomaly and Mie resonances of a single NP. By tailoring the configuration of the array and the shape of constituents, the *lattice* Kerker effect can be observed. The lattice Kerker effect arises due to interaction between lattice modes (i.e., CLRs) and resonances in a single NP, while the conventional Kerker effect is based on resonances in a single NP. We emphasize that the lattice Kerker effect is heavily studied in *all-dielectric* nanostructures with strong magnetic dipole (or quadrupole) resonances [34–37] with only one exception of arrays of relatively large *plasmonic* Au NPs exhibiting the Kerker effect at 750 nm [38]. Rapidly developing aluminum plasmonics [39–41] provides a solid ground for CLRs [42–46], but most of the studies are traditionally limited to purely electric interactions, either dipole or dipole-quadrupole [42]. In our recent work [47], we have shown that plasmonic arrays of Al NPs, very much similar to all-dielectric nanostructures, support magnetic dipole or quadrupole CLRs. We take the advantage of this property and demonstrate the Kerker effect in *plasmonic* Al metasurfaces. It is worth noting that Al is the only plasmonic material that manifests localized surface plasmon resonance in the UV wavelength range.

II. THEORY

The lattice Kerker effect in regular arrays of NPs can be understood as follows. Consider a plane wave with frequency

*gerasimov@icm.krasn.ru
†spolyutov@sfu-kras.ru

 ©2021 American Physical Society

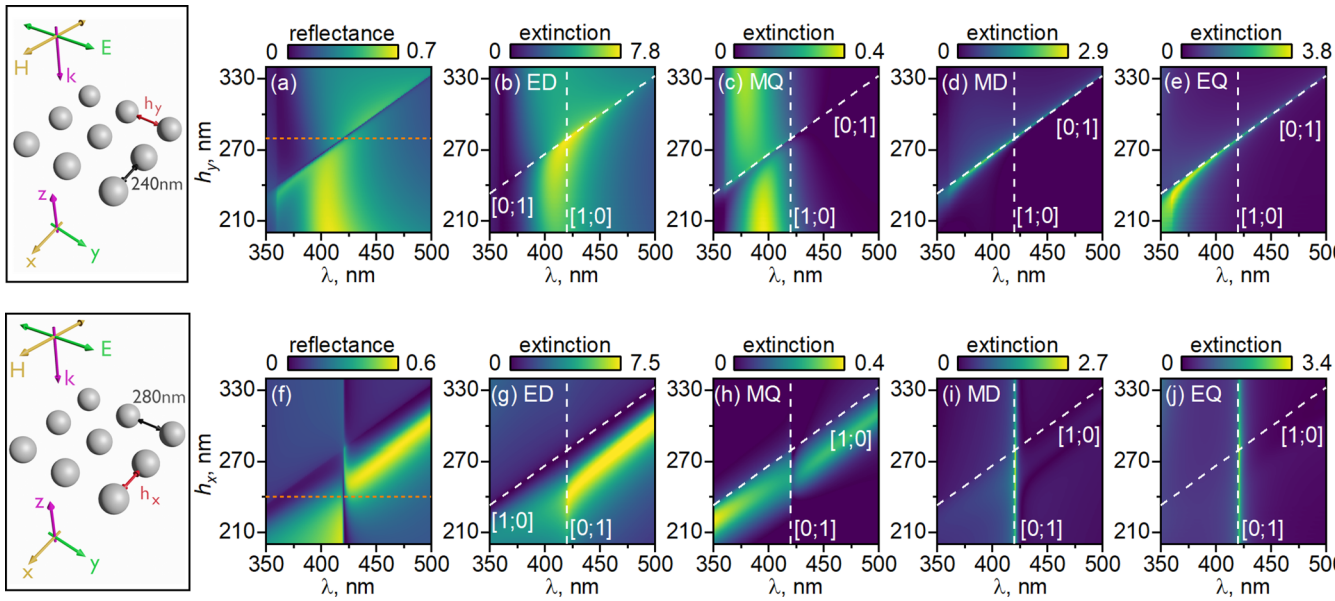

FIG. 1. (a),(f) Reflectance spectra, and (b)–(e), (g)–(j) multipole (ED, MQ, MD, EQ) decomposition of extinction efficiency for arrays with fixed $h_x = 240$ nm and different h_y (top), and with fixed $h_y = 280$ nm and different h_x (bottom). Al NPs with radius $R = 60$ nm have been considered in all cases. Notice a suppression of reflection which follows [0;1] RA, $\lambda_{RA} = \sqrt{\varepsilon_h} h_y$ [see Fig. 2(a) for details]. The order of the multipoles appearance is chosen for the sake of consistency with Eq. (5). Tabulated values of Al permittivity from Ref. [48] are used in simulations.

ω and a wave vector $|\mathbf{k}| = k = \sqrt{\varepsilon_h}\omega/c$ normally incident on a regular infinite array of NPs embedded in a homogeneous medium with permittivity ε_h (see the sketch in Fig. 1). In this case, each NP becomes indistinguishable from each other in terms of induced ℓ-th multipoles. The dependence of the Mie coefficients on the particle radius shows that the amplitude of the magnetic quadrupole is relatively small and higher-order modes can be ignored. The latter gives one the possibility to restrict the discussion by $\ell = 1$ and $\ell = 2$ fundamental modes, i.e., electric dipole (ED), **d**, magnetic dipole (MD), **m**, electric quadrupole (EQ), **D**, and magnetic quadrupole (MQ), **M**.

The electric field in the far field reads as [49]

$$\mathbf{E}_{sc} = -\frac{\omega^2}{c^2 r}\Big([[\mathbf{d}\times\mathbf{n}]\times\mathbf{n}] - [\mathbf{m}\times\mathbf{n}] - \frac{i\omega}{6c}([[\mathbf{D}\times\mathbf{n}]\times\mathbf{n}] - [\mathbf{M}\times\mathbf{n}])\Big)e^{ikr}. \quad (1)$$

Here r is the distance to the observation point and $\mathbf{n}$ is the unit vector pointing to the observation point. Cartesian components of EQ and MQ are $D_a = D_{ab}n_b$, $M_a = M_{ab}n_b$ (summation over repeating indices is implied), where $a, b = x, y, z$. In the particular case of an incident electric field polarized along the y axis, d_x, m_y, D_{xz}, and M_{yz} are all equal to zero. Thus, after introducing shorthands $d = d_y$, $m = m_x$, $D = D_{yz}$, and $M = M_{xz}$, the reflected field is

$$E_{\text{ref}} = \frac{\omega^2}{c^2 r}\Big[d - m + \frac{i\omega}{6c}(-D + M)\Big]e^{ikr}. \quad (2)$$

Dipole and quadrupole moments from the equation above can be found as $d = \tilde{\alpha}_d E_{\text{inc}}$, $m = \tilde{\alpha}_m H_{\text{inc}}$, $D = \tilde{\alpha}_D \nabla_z E_{\text{inc}}$, $M = \tilde{\alpha}_M \nabla_z H_{\text{inc}}$, where $\tilde{\alpha}$ are the respective effective polarizabilities, which depend on the geometry of the array:

$$\tilde{\alpha}_d = i\frac{3\varepsilon_h}{2k^3}\tilde{a}_1, \quad \tilde{\alpha}_M = i\frac{15\varepsilon_h^{3/2}}{k^5}\tilde{b}_2,$$
$$\tilde{\alpha}_m = i\frac{3\varepsilon_h}{2k^3}\tilde{b}_1, \quad \tilde{\alpha}_D = i\frac{15\varepsilon_h^{3/2}}{k^5}\tilde{a}_2, \quad (3)$$

where $\tilde{a}_\ell$ and $\tilde{b}_\ell$ are expansion coefficients that take into account the interaction between NPs (not to be confused with the expansion coefficients for a single NP). For a discussion on magnetic polarizability, see Appendix A. We emphasize that effective polarizabilities in the equation above depend on the properties of the individual constituent and on the lattice geometry, and also capture cross interactions between dipoles and quadrupoles [50].

For a plane wave considered here, $H_{\text{inc}} = \varepsilon_h E_{\text{inc}}$ and $\nabla_z E_{\text{inc}} = ikE_{\text{inc}}$, thus Eq. (2) can be rephrased as

$$E_{\text{ref}} = \frac{\omega^2}{c^2 r}\Big[\tilde{\alpha}_d - \tilde{\alpha}_m + \frac{k\omega}{6c}(-\tilde{\alpha}_D + \tilde{\alpha}_M)\Big]E_0 e^{ikr}. \quad (4)$$

It can be seen from Eq. (4) that the reflection is suppressed if the expression in square brackets is zero. Thus, by appropriately tailoring both NPs properties and their arrangement, the lattice Kerker effect may emerge.

III. RESULTS

We demonstrate the lattice Kerker effect in regular arrays of Al NPs embedded in a homogeneous environment with $\varepsilon_h = 2.25$. In a real experiment such a structure corresponds to NPs deposited onto a glass substrate and subsequently covered with a PMMA layer [43]. It is of critical importance to match refractive indices of substrate and interparticle host medium (superstrate), to have CLRs not vanished [51]. NPs

are arranged in infinite regular 2D lattice with periods h_x and h_y. The array is illuminated from the top by the plane wave with normal incidence along the z axis and polarization along the y axis. Narrowband suppression of the reflection can be observed in Figs. 1(a) and 1(f). We elaborate on this observation by plotting the contributions of each ℓ-th mode (electric and magnetic) to the reflection in Figs. 1(b)–1(e) and 1(g)–1(j) [higher-order $\ell \geqslant 3$ modes have been taken into account in Figs. 1(a) and 1(f), but are negligible). To do so, we consider the extinction efficiency that is proportional only to the real part of the expression in square brackets in Eq. (4). We justify this choice as follows. On using the equations for polarizabilities (3) and recalling that extinction efficiencies for electric and magnetic ℓ-th mode are proportional to real parts of the expansion coefficients, $Q^e_{\text{ext};\ell} \propto (2\ell+1)\Re(\tilde{a}_\ell)$ and $Q^m_{\text{ext};\ell} \propto (2\ell+1)\Re(\tilde{b}_\ell)$, the Kerker condition can be reformulated as

$$Q^e_{\text{ext};1} + Q^m_{\text{ext};2} - Q^m_{\text{ext};1} - Q^e_{\text{ext};2} = 0\,. \tag{5}$$

Keeping in mind that both real and imaginary parts of the expression in square brackets in Eq. (4) are anticipated to be zero for a case of suppressed backscattering, we shall limit the discussion only to a real part captured by the extinction efficiency, Eq. (5). The procedure for calculating extinction efficiency corresponding to each ℓ-th mode from the equation above is described in Appendix B.

Figures 1(b)–1(e) and 1(g)–1(j) show that spectral properties of two-dimensional (2D) arrays are tailored by varying one of the periods while keeping the other one constant [32,52]. In particular, the variation of h_x keeping $h_y = \text{const}$ yields in control of the [1; 0] Rayleigh anomaly (RA) $\lambda_{\text{RA}} = \sqrt{\varepsilon_h} h_x$ and adjusts the position of ED and MQ modes. The variation of h_y and $h_x = \text{const}$ adjusts [0; 1] RA: $\lambda_{\text{RA}} = \sqrt{\varepsilon_h} h_y$, which controls the MD and EQ modes. Thus, Figs. 1(b)–1(e) clearly shows that ED and MQ resonances are coupled to [1; 0] RA, while MD and EQ are coupled to [0; 1] RA. Noteworthy, is that the cross interaction between different modes [50,53] results in the emergence of additional minima and maxima in Figs. 1(b)–1(e) and 1(g)–1(j). Full suppression of reflection occurs when the spectral position of resonances corresponding to different anomalies coincide with each other and the total contribution of MD and EQ modes is equal to the contribution of ED and MQ modes.

This effect is clearly visible in Fig. 2(b), which shows the phases of the reflected wave created by individual multipoles. It can be seen from this figure that at $\lambda = 420$ nm, phases of the ED and MQ are close to zero while the phases of the EQ and MD are near to π. This means that the multipoles are in antiphase and destructively interfere with each other at the wavelength of the Kerker effect. It should be noted that this condition is not fulfilled near the [1; 0] RA.

It can be clearly seen in Fig. 2(a) that the reflection is completely suppressed at wavelengths close to [0; 1] RA. Moreover, the lattice Kerker effect can be also achieved for NPs with different R arranged in 2D lattices with properly chosen h_x and h_y. Thus, a complete suppression of backscattering can be tailored across UV and visible wavelength ranges, as shown in Fig. 2(a). As it was shown in our recent paper [[47], Fig. 6], the increase of the NP radius is

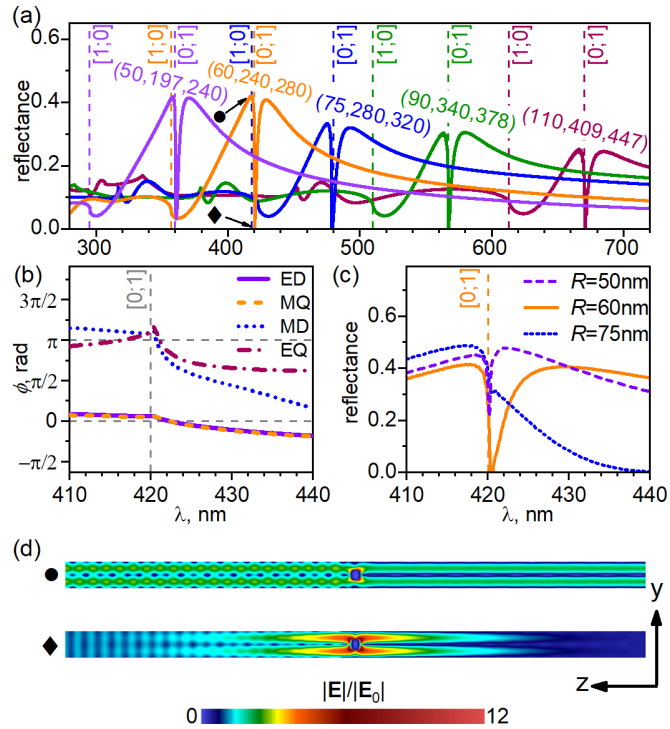

FIG. 2. (a) Reflectance for arrays with different geometrical parameters (R, h_x, h_y) as marked in the legend. Vertical dashed lines show respective spectral positions of [1; 0] and [0; 1] RAs for each array. (b) Multipole decomposition of the phase of the reflection amplitude $\phi = \arg(E_{\text{ref}})$ Eq. (2)] for NPs array with (60, 240, 280) nm [cf. orange line in (a)]. Notice the $\Delta\phi = \pi$ phase difference between EQ and MD contributions on one hand, and ED and MQ counterparts on the other hand, at $\lambda = \sqrt{\varepsilon_h} h_y$, the wavelength of the lattice Kerker effect. (c) Reflectance for arrays with different NP radii R and fixed $h_x = 240$ nm, $h_y = 280$ nm. (d) Electric field distribution in the ZY plane for (60, 240, 280) nm array at $\lambda = 417.6$ nm (top, maximum reflectance) and $\lambda = 420.5$ nm (bottom, zero reflectance). Notice rapidly vanishing reflected and transmitted fields at $\lambda = 420.5$ nm in the far zone due to strong localization of the electric field in the vicinity of NP, and high absorption shown in Fig. 3. The dynamics of the electromagnetic field propagation at both wavelengths is demonstrated in the Supplemental Material [66].

accompanied by the long-wavelength shift of ED, MD, EQ, MQ modes with their simultaneous broadening. Similar behavior of the modes should be expected for the array configurations in Fig. 2(a). This dependence is shown in Fig. 2(c) for arrays with different NP radii R and $h_x = 240$ nm, $h_y = 280$ nm. It can be seen that with increase of the NP radius, the suppressed reflectance range shifts to the long-wavelength range and broadens. To get more insight, we plot in Fig. 2(d) the amplitude of electric field in the ZY plane for the unit cell of the array with $h_x = 240$ nm, $h_y = 280$ nm, at $\lambda = 420.5$, which corresponds to zero reflection. For comparison, we also show the respective electric field distribution at $\lambda = 417.5$ nm, which corresponds to the maximum reflectance. In the case of a maximum reflection, the standing wave originates from the interference between incident and reflected wave of comparable amplitudes. For a zero reflectance, a symmetrical field distribution around a particle without an interference is

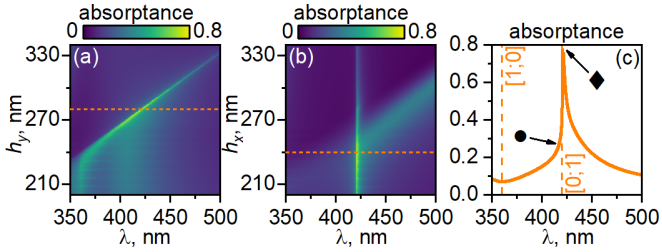

FIG. 3. Absorption spectra for arrays with the same parameters as in Fig. 1, i.e., for varying (a) h_y and (b) h_x, and (c) for array with $h_x = 240$ nm and $h_y = 280$ nm. Dashed horizontal lines indicate the lattice periods at which the absorption spectral line $\lambda = 420.5$ nm (c) is observed.

observed. In this case, the amplitude of the far field rapidly vanishes along the Z axis according to Eq. (2), in contrast to the case of a standing wave at $\lambda = 417.5$ nm. Thus, at $\lambda = 420.5$, i.e., in the lattice Kerker regime, we are left only with the incident field in the far zone in the backscattering direction.

Noteworthy, is that the electric field enhancement near NP is significantly larger for the case of suppressed reflection due to overlapping of the ED, EQ, MD, and MQ modes at the corresponding wavelength. Thus, the Kerker effect in plasmonic arrays is accompanied by high absorption of the electromagnetic energy shown in Fig. 3, up to 80%. The latter feature is generally not observed in weakly absorbing dielectric structures [34], except a few cases for amorphous [54] or crystalline [55] silicon.

IV. SUMMARY

We have demonstrated the lattice Kerker effect in plasmonic arrays of Al nanoparticles, whereas for *single* lossy NPs it is, in principle, impossible to achieve within a framework of dipole approximation [20]. The plasmonic lattice Kerker effect is based on the interference suppression of dominant ED radiation (with negligible MQ impact) by the cumulative contribution of the fields produced by MD and EQ that is introduced in classical electrodynamics [49]. We show that a complete suppression of the backscattering can be tuned within the UV and visible spectral ranges by varying geometry of arrays, i.e., radius of NPs and the distance between them. High absorption and strong electric field localization are observed at the frequency that corresponds to the lattice Kerker effect.

The lattice Kerker effect can also be observed in other metals besides aluminum under strict adherence to a number of conditions: it was shown in Ref. [38] that regular arrays of Au NPs also demonstrate resonant suppression of reflection at the border of the IR range at $\lambda = 750$ nm. Obviously, the effect can be also predicted in the IR range using large particles ($R > 100$ nm) and with a large lattice period. In this sense, gold differs just a little in comparison to all-dielectric materials that manifest the Kerker effect only in the IR spectral range.

Utilization of aluminum completely eliminates spectral restrictions and makes it possible to create conditions for the manifestation of the Kerker effect both in the entire visible and in the long-wavelength range of the UV spectrum. We believe that aluminum opens the possibilities of employing the Kerker effect in a set of different applications as is discussed below. For example, it can be used in spectroscopy of biomaterials with characteristic absorption bands in UV spectral range, in photocatalysis [56] and in studies of organic and biological systems [57] that exhibit strong UV absorption. Arrays of Al NPs also provide the possibility of selective suppression of intense lines of undesirable radiation. The latter property is of critical importance for ultra-narrowband absorption [58] and surface-enhanced Raman spectroscopy [59,60]. Selective suppression of background radiation at the excitation laser wavelength is important for studies of luminescence spectra or Raman spectra [61]. This problem can be solved by using arrays of Al NPs as optical filters using the backscattering suppression within one high-Q spectral line. The effect can be useful in applications related to cloaking, where there is the requirement to expand the spectral range with effective suppression of radiation from a surface.

It is argued that our results expand the list of materials for fabrication of photonic devices for short-wavelength spectral range and have academic interest of its own being a theoretical prediction of the Kerker effect utilizing the broad spectral range in plasmonic materials.

ACKNOWLEDGMENTS

The research was supported by the Ministry of Science and High Education of Russian Federation, Project No. FSRZ-2020-0008, by RFBR, Krasnoyarsk Territory and Krasnoyarsk Regional Fund of Science, project number 20-42-240003 and by the Russian Science Foundation (Project No. 18-13-00363) (numerical calculations of phase dependences and corresponding research), A. E. acknowledges the grant of the President of the Russian Federation, agreement No. 075–15–2019–676.

APPENDIX A: MAGNETIC POLARIZABILITY

It is a well-known fact that magnetic permeability at optical frequencies is almost equal to 1 (moreover, it is not quite clear what is the magnetic permeability at these frequencies at all) [[62], Chap. 79]. Therefore, the mechanism underlying the emergence of a magnetic moment at these frequencies is the interaction of an electric field with matter. Under a electromagnetic wave (in our case, a plane incident wave and at least a locally plane scattered wave in the far field), we imply the entire electromagnetic field, not its separate components. Since the wave vector and one of the field amplitude vectors (electric or magnetic) fully determine the wave, and the remaining vector is fully determined by the other two, we can safely operate with the electric or magnetic field amplitude vector at our discretion. We may write the magnetic dipole moment in terms of an electric field, but they would be connected by a pseudotensor of the second rank, not a scalar, as it is in our case. This is simply inconvenient, so we choose a more convenient representation, which does not affect the obtained results.

Polarizability is generally defined as the tensor connecting the external field and the corresponding dipole moment. For

the case of magnetic moment

$$m_i = \alpha_{ij} H_j^0 \,. \tag{A1}$$

Since **M** is linearly dependent on $\mathbf{H}^0$, and **P** is linearly dependent on **E**, Eq. (B2) can be rewritten as:

$$m_i = A_{ij} H_j^0 + B_{ij} E_j^0 \,. \tag{A2}$$

Here A_{ij}, B_{ij} are linear operators that depend on the properties of the particle and the array geometry. For a plane electromagnetic wave $\mathbf{E} = \varepsilon_h^{-1/2}[\mathbf{H}^0 \times \mathbf{n}]$. Thus we get

$$m_i = \left(\alpha_{ij}^1 + \alpha_{ij}^2\right) H_j^0 = \alpha_{ij} H_j^0, \tag{A3}$$

where $\alpha_{ij}^1 = A_{ij}$, $\alpha_{ij}^2 = \varepsilon_h^{-1/2} \epsilon_{mjl} n_l B_{im}$, ϵ_{mjl} is the Levi-Civita symbol. Tensor α_{ij} is nothing but the familiar magnetic dipole polarizability. The second term cannot be ignored for most materials in the optical range, and even more, $\alpha_{ij}^2 \gg \alpha_{ij}^1$. So in our case we assume $\alpha_{ij}^1 = 0$. Due to the symmetry of the system in our case $\alpha_{ij} = \alpha_m \delta_{ij}$, which gives the expression for the magnetic dipole used in the paper.

APPENDIX B: MULTIPOLE FIELD DECOMPOSITION

The total field **E** and the reflectance spectra are calculated with the commercial Finite-Difference Time-Domain package [63]. A Standard approach is used to mimic infinite 2D periodic structures [33,43,47,64]: periodic boundary conditions have been applied at the lateral boundaries of the simulation box, while perfectly matched layer boundary conditions were used on the remaining top and bottom sides. Reflectance is calculated at the top of the simulation box. An adaptive mesh is used to reproduce accurately the nanosphere shape. Multipole decomposition of the extinction efficiency from Eq. (5) is calculated from the spatial electromagnetic field distribution as described in Ref. [65]. Namely, The electric dipole moment is defined by the simple equation [49]

$$\mathbf{d} = \iiint_V \mathbf{P} d^3\mathbf{r}. \tag{B1}$$

The magnetic dipole moment in the general case in the time representation reads as follows:

$$\mathbf{m} = \int_V \mathbf{M} dV + \frac{1}{2c} \int_V \left[\mathbf{r} \times \frac{\partial \mathbf{P}}{\partial t}\right] dV, \tag{B2}$$

where M is magnetization. Since in the optics for the most materials magnetic susceptibility is small [62], the first term in the right side of the equation can be ignored. Thus, in the complex representation we obtain an expression for the magnetic dipole moment:

$$\mathbf{m} = i\frac{k}{2} \iiint_V [\mathbf{P} \times \mathbf{r}] d^3\mathbf{r}. \tag{B3}$$

Similar expressions can be obtained for quadrupole moments:

$$\hat{\mathbf{D}} = 3 \iiint_V (\mathbf{P} \otimes \mathbf{r} + \mathbf{r} \otimes \mathbf{P}) d^3\mathbf{r},$$
$$\hat{\mathbf{M}} = \frac{2}{3} ik \iiint_V \mathbf{r} \otimes [\mathbf{P} \times \mathbf{r}] d^3\mathbf{r}, \tag{B4}$$

where ε is permittivity of the particles, $\mathbf{P} = (\varepsilon - 1)/4\pi\mathbf{E}$ is polarization density, and k is the wave number. The corresponding extinction cross sections read as follows:

$$\sigma_{ext}^d = \frac{4\pi k}{\sqrt{\varepsilon_h}|\mathbf{E}_0|^2} \Im(\mathbf{E}_0^* \cdot \mathbf{d}),$$
$$\sigma_{ext}^m = \frac{4\pi k}{\sqrt{\varepsilon_h}|\mathbf{H}_0|^2} \Im(\mathbf{H}_0^* \cdot \mathbf{m}),$$
$$\sigma_{ext}^D = -\frac{\pi k}{3\sqrt{\varepsilon_h}|\mathbf{E}_0|^2} \Im[(\nabla \otimes \mathbf{E}_0^* + \mathbf{E}_0^* \otimes \nabla) : \hat{D}],$$
$$\sigma_{ext}^M = -\frac{2\pi k}{\sqrt{\varepsilon_h}|\mathbf{H}_0|^2} \Im[(\nabla \otimes \mathbf{H}_0^* + \mathbf{H}_0^* \otimes \nabla) : \hat{M}], \tag{B5}$$

where $\mathbf{E}_0$ and $\mathbf{H}_0$ are components of the incident electromagnetic field. The respective extinction efficiency Q is defined as the extinction cross section σ normalized to the geometric cross section πR^2 of a single particle with radius R.

[1] M. Kerker, D.-S. Wang, and C. L. Giles, Electromagnetic scattering by magnetic spheres, J. Opt. Soc. Am. **73**, 765 (1983).

[2] I. Staude, T. Pertsch, and Y. S. Kivshar, All-dielectric resonant meta-optics lightens up, ACS Photonics **6**, 802 (2019).

[3] A. B. Evlyukhin, S. M. Novikov, U. Zywietz, R. L. Eriksen, C. Reinhardt, S. I. Bozhevolnyi, and B. N. Chichkov, Demonstration of magnetic dipole resonances of dielectric nanospheres in the visible region, Nano Lett. **12**, 3749 (2012).

[4] Y. H. Fu, A. I. Kuznetsov, A. E. Miroshnichenko, Y. F. Yu, and B. Luk'yanchuk, Directional visible light scattering by silicon nanoparticles, Nat. Commun. **4**, 1527 (2013).

[5] S. Person, M. Jain, Z. Lapin, J. J. Sáenz, G. Wicks, and L. Novotny, Demonstration of zero optical backscattering from single nanoparticles, Nano Lett. **13**, 1806 (2013).

[6] I. Staude, A. E. Miroshnichenko, M. Decker, N. T. Fofang, S. Liu, E. Gonzales, J. Dominguez, T. S. Luk, D. N. Neshev, I. Brener, and Y. Kivshar, Tailoring directional scattering through magnetic and electric resonances in subwavelength silicon nanodisks, ACS Nano **7**, 7824 (2013).

[7] R. Alaee, R. Filter, D. Lehr, F. Lederer, and C. Rockstuhl, A generalized kerker condition for highly directive nanoantennas, Opt. Lett. **40**, 2645 (2015).

[8] F. Shen, N. An, Y. Tao, H. Zhou, Z. Jiang, and Z. Guo, Anomalous forward scattering of gain-assisted dielectric shell-coated metallic core spherical particles, Nanophotonics **6**, 1063 (2016).

[9] P. D. Terekhov, K. V. Baryshnikova, A. S. Shalin, A. Karabchevsky, and A. B. Evlyukhin, Resonant forward scattering of light by high-refractive-index dielectric nanoparticles with toroidal dipole contribution, Opt. Lett. **42**, 835 (2017).

[10] P. R. Wiecha, A. Cuche, A. Arbouet, C. Girard, G. C. des Francs, A. Lecestre, G. Larrieu, F. Fournel, V. Larrey, T. Baron, and V. Paillard, Strongly directional scattering from dielectric nanowires, ACS Photonics **4**, 2036 (2017).

[11] Y. Yang, A. E. Miroshnichenko, S. V. Kostinski, M. Odit, P. Kapitanova, M. Qiu, and Y. S. Kivshar, Multimode directionality in all-dielectric metasurfaces, Phys. Rev. B **95**, 165426 (2017).

[12] M. Q. Liu and C. Y. Zhao, Lattice invisibility effect based on transverse Kerker scattering in 1D metalattices, J. Phys. D **52**, 495107 (2019).

[13] H. Barhom, A. A. Machnev, R. E. Noskov, A. Goncharenko, E. A. Gurvitz, A. S. Timin, V. A. Shkoldin, S. V. Koniakhin, O. Y. Koval, M. V. Zyuzin, A. S. Shalin, I. I. Shishkin, and P. Ginzburg, Biological Kerker effect boosts light collection efficiency in plants, Nano Lett. **19**, 7062 (2019).

[14] D. Pan, T. Feng, W. Zhang, and A. A. Potapov, Unidirectional light scattering by electric dipoles induced in plasmonic nanoparticles, Opt. Lett. **44**, 2943 (2019).

[15] H. K. Shamkhi, K. V. Baryshnikova, A. Sayanskiy, P. Kapitanova, P. D. Terekhov, P. Belov, A. Karabchevsky, A. B. Evlyukhin, Y. Kivshar, and A. S. Shalin, Transverse Scattering and Generalized Kerker Effects in All-Dielectric Mie-Resonant Metaoptics, Phys. Rev. Lett. **122**, 193905 (2019).

[16] C. Liu, L. Chen, T. Wu, Y. Liu, R. Ma, J. Li, Z. Yu, H. Ye, and L. Yu, Characteristics of electric quadrupole and magnetic quadrupole coupling in a symmetric silicon structure, New J. Phys. **22**, 023018 (2020).

[17] A. Bag, M. Neugebauer, P. Woźniak, G. Leuchs, and P. Banzer, Transverse Kerker Scattering for Angstrom Localization of Nanoparticles, Phys. Rev. Lett. **121**, 193902 (2018).

[18] M. Dubois, L. Leroi, Z. Raolison, R. Abdeddaim, T. Antonakakis, J. de Rosny, A. Vignaud, P. Sabouroux, E. Georget, B. Larrat, G. Tayeb, N. Bonod, A. Amadon, F. Mauconduit, C. Poupon, D. LeBihan, and S. Enoch, Kerker Effect in Ultrahigh-field Magnetic Resonance Imaging, Phys. Rev. X **8**, 031083 (2018).

[19] W. Liu and Y. S. Kivshar, Generalized Kerker effects in nanophotonics and meta-optics [invited], Opt. Express **26**, 13085 (2018).

[20] J. Olmos-Trigo, C. Sanz-Fernández, D. R. Abujetas, J. Lasa-Alonso, N. de Sousa, A. García-Etxarri, J. A. Sánchez-Gil, G. Molina-Terriza, and J. J. Sáenz, Kerker Conditions Upon Lossless, Absorption, and Optical Gain Regimes, Phys. Rev. Lett. **125**, 073205 (2020).

[21] Q. Yang, W. Chen, Y. Chen, and W. Liu, Ideal Kerker scattering by homogeneous spheres: the role of gain or loss, arXiv:2009.04939.

[22] E. Poutrina, A. Rose, D. Brown, A. Urbas, and D. R. Smith, Forward and backward unidirectional scattering from plasmonic coupled wires, Opt. Express **21**, 31138 (2013).

[23] A. Pors, S. K. H. Andersen, and S. I. Bozhevolnyi, Unidirectional scattering by nanoparticles near substrates: generalized kerker conditions, Opt. Express **23**, 28808 (2015).

[24] M. Kataja, S. Pourjamal, N. Maccaferri, P. Vavassori, T. K. Hakala, M. J. Huttunen, P. Törmä, and S. van Dijken, Hybrid plasmonic lattices with tunable magneto-optical activity, Opt. Express **24**, 3652 (2016).

[25] M. B. Ross, C. A. Mirkin, and G. C. Schatz, Optical properties of one-, two-, and three-dimensional arrays of plasmonic nanostructures, J. Phys. Chem. C **120**, 816 (2016).

[26] V. G. Kravets, A. V. Kabashin, W. L. Barnes, and A. N. Grigorenko, Plasmonic surface lattice resonances: a review of properties and applications, Chem. Rev. **118**, 5912 (2018).

[27] S. Zou, N. Janel, and G. C. Schatz, Silver nanoparticle array structures that produce remarkably narrow plasmon lineshapes, J. Chem. Phys. **120**, 10871 (2004).

[28] V. A. Markel, Divergence of dipole sums and the nature of non-Lorentzian exponentially narrow resonances in one-dimensional periodic arrays of nanospheres, J. Phys. B **38**, L115 (2005).

[29] B. Auguié and W. L. Barnes, Collective Resonances in Gold Nanoparticle Arrays, Phys. Rev. Lett. **101**, 143902 (2008).

[30] V. G. Kravets, F. Schedin, and A. N. Grigorenko, Extremely Narrow Plasmon Resonances Based on Diffraction Coupling of Localized Plasmons in Arrays of Metallic Nanoparticles, Phys. Rev. Lett. **101**, 087403 (2008).

[31] A. B. Evlyukhin, C. Reinhardt, A. Seidel, B. S. Luk'yanchuk, and B. N. Chichkov, Optical response features of Si-nanoparticle arrays, Phys. Rev. B **82**, 045404 (2010).

[32] J. Li, N. Verellen, and P. Van Dorpe, Engineering electric and magnetic dipole coupling in arrays of dielectric nanoparticles, J. Appl. Phys. **123**, 083101 (2018).

[33] A. D. Utyushev, I. L. Isaev, V. S. Gerasimov, A. E. Ershov, V. I. Zakomirnyi, I. L. Rasskazov, S. P. Polyutov, H. Ågren, and S. V. Karpov, Engineering novel tunable optical high-q nanoparticle array filters for a wide range of wavelengths, Opt. Express **28**, 1426 (2020).

[34] V. E. Babicheva and A. B. Evlyukhin, Resonant lattice Kerker effect in metasurfaces with electric and magnetic optical responses, Laser Photonics Rev. **11**, 1700132 (2017).

[35] V. E. Babicheva and J. V. Moloney, Lattice effect influence on the electric and magnetic dipole resonance overlap in a disk array, Nanophotonics **7**, 1663 (2018).

[36] V. E. Babicheva, Lattice Kerker effect in the array of hexagonal boron nitride antennas, MRS Adv. **3**, 2783 (2018).

[37] V. E. Babicheva and A. B. Evlyukhin, Resonant suppression of light transmission in high-refractive-index nanoparticle metasurfaces, Opt. Lett. **43**, 5186 (2018).

[38] V. E. Babicheva and A. B. Evlyukhin, Metasurfaces with electric quadrupole and magnetic dipole resonant coupling, ACS Photonics **5**, 2022 (2018).

[39] G. Maidecchi, G. Gonella, R. Proietti Zaccaria, R. Moroni, L. Anghinolfi, A. Giglia, S. Nannarone, L. Mattera, H.-L. Dai, M. Canepa, and F. Bisio, Deep ultraviolet plasmon resonance in aluminum nanoparticle arrays, ACS Nano **7**, 5834 (2013).

[40] M. W. Knight, N. S. King, L. Liu, H. O. Everitt, P. Nordlander, and N. J. Halas, Aluminum for plasmonics, ACS Nano **8**, 834 (2014).

[41] D. Gérard and S. K. Gray, Aluminium plasmonics, J. Phys. D **48**, 184001 (2015).

[42] A. Yang, A. J. Hryn, M. R. Bourgeois, W.-K. Lee, J. Hu, G. C. Schatz, and T. W. Odom, Programmable and reversible plasmon mode engineering, Proc. Natl. Acad. Sci. **113**, 14201 (2016).

[43] D. Khlopin, F. Laux, W. P. Wardley, J. Martin, G. A. Wurtz, J. Plain, N. Bonod, A. V. Zayats, W. Dickson, and D. Gérard, Lattice modes and plasmonic linewidth engineering in gold and aluminum nanoparticle arrays, J. Opt. Soc. B **34**, 691 (2017).

[44] M. Esposito, F. Todisco, S. Bakhti, A. Passaseo, I. Tarantini, M. Cuscunà, N. Destouches, and V. Tasco, Symmetry breaking in oligomer surface plasmon lattice resonances, Nano Lett. **19**, 1922 (2019).

[45] Y. Kawachiya, S. Murai, M. Saito, K. Fujita, and K. Tanaka, Photoluminescence decay rate of an emitter layer on an Al nanocylinder array: effect of layer thickness, J. Opt. Soc. B **36**, E1 (2019).

[46] X. Zhu, G. M. Imran Hossain, M. George, A. Farhang, A. Cicek, and A. A. Yanik, Beyond noble metals: High Q-factor aluminum nanoplasmonics, ACS Photonics **7**, 416 (2020).

[47] A. E. Ershov, V. S. Gerasimov, R. G. Bikbaev, S. P. Polyutov, and S. V. Karpov, Mode coupling in arrays of Al nanoparticles, J. Quant. Spectrosc. Radiat. Transfer **248**, 106961 (2020).

[48] D. Smith, E. Shiles, and M. Inokuti, The Optical Properties of Metallic Aluminum, in *Handbook of Optical Constants of Solids*, edited by E. D. Palik (Academic Press, Burlington, VT, 1997), pp. 369–406.

[49] L. D. Landau and E. M. Lifshitz, *The Classical Theory of Fields*, 4th ed., Course of Theoretical Physics, Vol. 2 (Butterworth-Heinemann, Oxford, 1987).

[50] V. E. Babicheva and A. B. Evlyukhin, Analytical model of resonant electromagnetic dipole-quadrupole coupling in nanoparticle arrays, Phys. Rev. B **99**, 195444 (2019).

[51] B. Auguié, X. M. Bendaña, W. L. Barnes, and F. J. García de Abajo, Diffractive arrays of gold nanoparticles near an interface: Critical role of the substrate, Phys. Rev. B **82**, 155447 (2010).

[52] V. I. Zakomirnyi, S. V. Karpov, H. Ågren, and I. L. Rasskazov, Collective lattice resonances in disordered and quasi-random all-dielectric metasurfaces, J. Opt. Soc. B **36**, E21 (2019).

[53] V. I. Zakomirnyi, A. E. Ershov, V. S. Gerasimov, S. V. Karpov, H. Ågren, and I. L. Rasskazov, Collective lattice resonances in arrays of dielectric nanoparticles: a matter of size, Opt. Lett. **44**, 5743 (2019).

[54] C.-Y. Yang, J.-H. Yang, Z.-Y. Yang, Z.-X. Zhou, M.-G. Sun, V. E. Babicheva, and K.-P. Chen, Nonradiating silicon nanoantenna metasurfaces as narrowband absorbers, ACS Photonics **5**, 2596 (2018).

[55] J. Tian, Q. Li, P. A. Belov, R. K. Sinha, W. Qian, and M. Qiu, High-Q all-dielectric metasurface: Super and suppressed optical absorption, ACS Photonics **7**, 1436 (2020).

[56] Y. Chen, X. Xin, N. Zhang, and Y.-J. Xu, Aluminum-based plasmonic photocatalysis, Part. Part. Syst. Charact. **34**, 1600357 (2017).

[57] I. Tanabe, Y. Y. Tanaka, K. Watari, T. Hanulia, T. Goto, W. Inami, Y. Kawata, and Y. Ozaki, Aluminum film thickness dependence of surface plasmon resonance in the far- and deep-ultraviolet regions, Chem. Lett. **46**, 1560 (2017).

[58] Z. Li, S. Butun, and K. Aydin, Ultranarrow band absorbers based on surface lattice resonances in nanostructured metal surfaces, ACS Nano **8**, 8242 (2014).

[59] S. K. Jha, Z. Ahmed, M. Agio, Y. Ekinci, and J. F. Löffler, Deep-UV surface-enhanced resonance Raman scattering of adenine on aluminum nanoparticle arrays, J. Am. Chem. Soc. **134**, 1966 (2012).

[60] B. Sharma, M. F. Cardinal, M. B. Ross, A. B. Zrimsek, S. V. Bykov, D. Punihaole, S. A. Asher, G. C. Schatz, and R. P. Van Duyne, Aluminum film-over-nanosphere substrates for deep-UV surface-enhanced resonance Raman spectroscopy, Nano Lett. **16**, 7968 (2016).

[61] D. A. Long, *The Raman Effect: A Unified Treatment of the Theory of Raman Scattering by Molecules* (Wiley, Chichester, UK, 2002), p. 584.

[62] L. D. Landau, L. P. Pitaevskii, and E. M. Lifshitz, *Electrodynamics of Continuous Media*, 2nd ed., Course of theoretical physics, Vol. 2 (Butterworth-Heinemann, Oxford, 1984).

[63] Lumerical Solutions, FDTD Solutions (2020).

[64] V. I. Zakomirnyi, I. L. Rasskazov, V. S. Gerasimov, A. E. Ershov, S. P. Polyutov, and S. V. Karpov, Refractory titanium nitride two-dimensional structures with extremely narrow surface lattice resonances at telecommunication wavelengths, Appl. Phys. Lett. **111**, 123107 (2017).

[65] A. B. Evlyukhin, C. Reinhardt, and B. N. Chichkov, Multipole light scattering by nonspherical nanoparticles in the discrete dipole approximation, Phys. Rev. B **84**, 235429 (2011).

[66] See Supplemental Material at http://link.aps.org/supplemental/10.1103/PhysRevB.103.035402 for details on the dynamics of the electromagnetic field propagation at 417.6 nm and 420.5 nm wavelengths.